

Time-Resolved Measurements of Plasma Parameters for Nanosecond-Pulsed Argon Plasmas

Connie Y. Liu¹, Morris B. Cohen¹, *Senior Member, IEEE*, and Mitchell L. R. Walker

Abstract—This article aims to understand the physics of pulsed plasmas by investigating the ionization and recombination of pulsed plasmas on the nanosecond timescale and how operating conditions affect the time-resolved electron temperature and electron density of a pulsed plasma. A nanosecond-pulsed argon plasma discharge was generated at various pulse frequencies, widths, and pressures. The argon emission lines were analyzed with a time-synchronized, intensified charge-coupled device (ICCD) spectrometer assembly that gated at 4 ns, and relative intensities of strong argon neutral and ion lines were used in line-ratio calculations. These experimentally determined ratios were compared to theoretical ratios generated from PrismSPECT, a collisional-radiative spectral analysis software, to obtain time-resolved electron temperature (~ 1 eV) and electron density ($10^{14} - 10^{15}$ cm⁻³) over the various operating conditions as well as to discover trends of these plasma parameters over the lifetime of the pulsed plasma. Increasing pulse repetition frequency of the plasma increased the value of maximum T_e , shortened the T_e rise and decay times, and increased the excited argon neutral population. While n_e was relatively independent of pulse frequency, higher pulse frequencies resulted in a faster n_e decay. Maximum T_e and n_e were weakly dependent on applied discharge voltage, but both parameters decayed sooner in time with increasing voltage. Lastly, T_e was inversely proportional to pressure, but n_e was approximately linear. All three pressures had similar but time-shifted temporal profiles for n_e . Plasmas in all operating conditions had ionization and recombination times in the tens of nanoseconds.

Index Terms—Argon plasma, electron density, electron temperature, nanosecond-pulsed discharge, optical emission spectroscopy (OES).

I. INTRODUCTION

THERE has been renewed interest recently in nanosecond-pulsed plasma discharges in enhancing and stabilizing combustion (i.e., shortening ignition delay times, extending extinction limits, improving flame stabilization, increasing flame speed, and suppressing soot

Manuscript received July 11, 2019; revised December 10, 2019; accepted January 8, 2020. Date of publication March 10, 2020; date of current version April 10, 2020. This work was supported in part by the Office of Naval Research (ONR) Young Investigator Program to the Georgia Institute of Technology under Award N00014-15-1-2526 and in part by the Defense Advanced Research Projects Agency (DARPA) to the Georgia Institute of Technology under Award HR0011-16- 2-0031. The work of Connie Y. Liu was supported by the National Science Foundation Graduate Research Fellowship (NSF GRF). The review of this article was arranged by Senior Editor R. P. Joshi. (*Corresponding author: Connie Y. Liu.*)

Connie Y. Liu and Mitchell L. R. Walker are with the School of Aerospace Engineering, Georgia Institute of Technology, Atlanta, GA 30332 USA (e-mail: cyliu@gatech.edu).

Morris B. Cohen is with the School of Electrical and Computer Engineering, Georgia Institute of Technology, Atlanta, GA 30332 USA.

Color versions of one or more of the figures in this article are available online at <http://ieeexplore.ieee.org>.

Digital Object Identifier 10.1109/TPS.2020.2973024

formation) [1], [2], biochemical decontamination by removing harmful gases via plasma [2], [3], and material processing and surface treatment applications such as depositing, etching, and coating [3]–[5]. Nanosecond-pulsed discharges can be used to effectively produce a stable plasma with a high concentration of metastable species, ions, and high-energy electrons [1], [5], and pulsed discharges require less input power—up to 250 times lower—than steady discharges to produce a plasma with the same electron density [3]. These types of plasma also provide more flexibility than steady plasmas because of the ability to control plasma parameters such as electron temperature and electron number density by changing the characteristics of the input voltage pulses.

In order to customize a pulsed plasma for the aforementioned applications, there is a need to understand the physics and dynamics through the lifetime of the plasma. This, therefore, requires knowledge about the nanosecond behavior of the plasma, such as time-resolved measurements of electron temperature and electron density. However, to date, there have not been any direct, time-resolved measurements of electron density and electron temperature for low-pressure (≈ 1 Torr), nanosecond pulsed (NSP) argon discharges. Similarly, there have only been a limited number of pulsed plasma dynamics experiments and theoretical models to simulate nanosecond, pulsed operation of low-pressure argon and to determine the evolution of plasma parameters during a pulse period [5], [6].

The focus of this article is on time-resolved measurements of electron temperature and electron density in nanosecond-pulsed argon discharges via optical emission spectroscopy. Argon was chosen for this article because of its inertness and low breakdown voltage, which allowed for a greater range of discharge voltage test conditions. The plasma discharge was generated in between two dome electrodes in a custom-made, Pyrex plasma cell, and the argon plasma emission light was analyzed with an intensified charge-coupled device (ICCD) camera–spectrometer assembly, designed to capture emission lines in 4-ns snapshots. The main objective of this article is to improve the current understanding of the plasma dynamics of nanosecond-pulsed plasmas through measuring the time evolution of electron temperature and electron density over the lifetime of a pulsed, argon plasma discharge.

II. EXPERIMENTAL SETUP

The experiments were conducted in a custom-made plasma cell and the corresponding vacuum components are shown in Fig. 1.

The handblown, Pyrex plasma cell had a 2.25-in outer diameter and was 9-in long with glass-to-steel ISO-type flanges

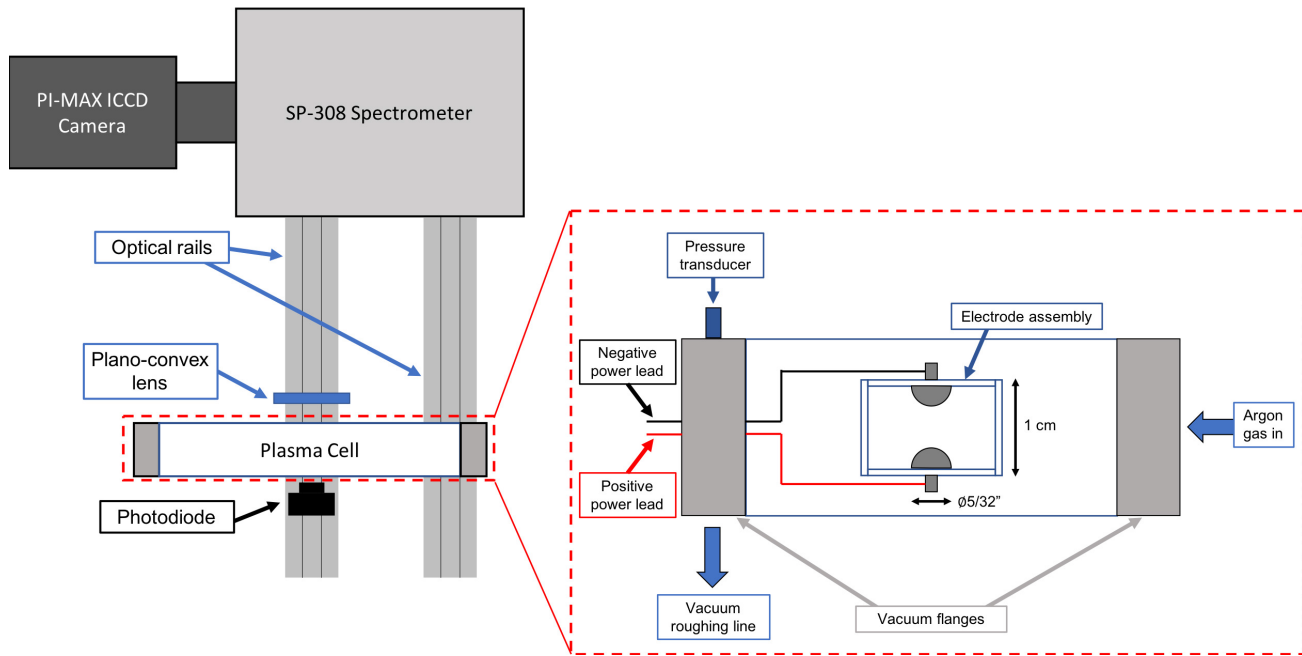


Fig. 1. Experimental setup with plasma cell, electrodes, diagnostics, and selected vacuum and optical system components.

on either end. The cell was attached to a 6-way and 4-way cross with 4.5-in ConFlat (CF) flanges, through which all the electrical connections were fed. The experimental setup was placed on a 3 ft \times 4 ft vibration-isolated optical table from Thorlabs. Nanosecond-pulsed argon plasma discharges were generated within the plasma cell via voltage breakdown.

The electrodes were fashioned from 5/32" \times 1/2" domed, anodized aluminum rivets threaded into rectangular, Macor ceramic plates (1.6" \times 1" \times 0.25" thick) and set 1 cm apart in a Macor mount with four 1/16" diameter alumina ceramic rods. The electrode assembly, seen in Fig. 2, was painted with Ceramabond 569 to lock the assembly together and to cover any exposed metal components as well as to provide additional insulation protection to the assembly. Slots were designed in the support structure to fit the high-voltage 22-AWG Cicoil wire.

Pressure in the plasma cell was monitored by a Kurt J. Lesker 375 Series Controller and a 275 Pirani gauge. An argon-calibrated 247D MKS Mass Flow Controller, a 200-sccm flowmeter, and an Arduino microcontroller controlled ultrahigh purity (99.999%) argon flow into the plasma cell.

An Eagle Harbor Technologies NSP-120-20F NSP capable of pulsing up to 10 kHz and supplying up to 20 kV with a minimum pulsewidth of 20 ns was used to generate the nanosecond-pulsed plasma. While the pulsewidth of the NSP was being fixed at 20 ns, the discharge voltage and pulse repetition frequency could be individually adjusted.

A. Time-Resolved Diagnostics

This article dealt with the design and implementation of a new plasma diagnostics system to temporally sweep and obtain nanosecond, time-resolved electron number density and electron temperature measurements of the plasma.

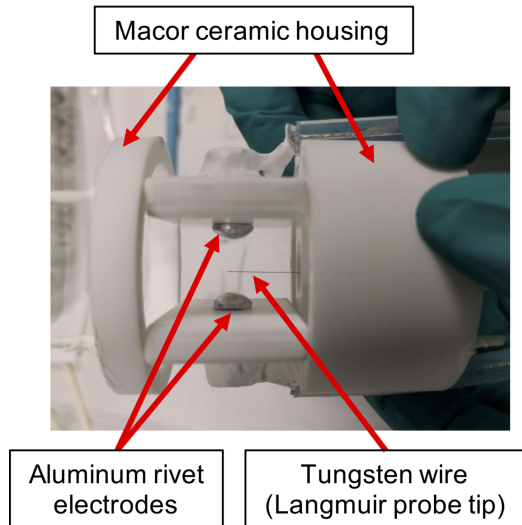


Fig. 2. Rivet electrodes in its Macor housing.

Current techniques to obtain time-resolved plasma parameters from a pulsed plasma include Langmuir probes, optical emission spectroscopy, laser diode spectroscopy, and Thomson scattering [4]. Thomson scattering gives direct insights into plasma properties with excellent spatial and temporal resolution, is noninvasive, and does not necessitate an equilibrium plasma [4]. It has been used in time-resolved measurements of nanosecond-pulsed discharges but requires specialized equipment and a hot (e.g., $T_e > 2$ eV), dense (e.g., above 10^{13} cm $^{-3}$) plasma [2], [4], [7]. The experimental plasma was predicted to have $n_e \sim \mathcal{O}(10^{14}$ cm $^{-3}$) and $T_e \sim \mathcal{O}(1$ eV), just within the range of Thomson scattering, but the necessary laser equipment was not available.

Langmuir probes are easy to build and implement but difficult to analyze and are intrusive diagnostic tools. The calculated electron density and temperature depend heavily on interpretation of Langmuir probe data, so high uncertainties are common [8].

Several groups have used tunable diode laser absorption spectroscopy (TDLAS) for time-resolved temperature and number density measurements in a pulsed argon plasma from the absorption spectra. However, those measurements were taken on a metastable argon species, and a detailed model was used to estimate or calculate electron temperature and electron number density [9]–[12]. TDLAS is an accurate diagnostic when looking at specific densities and gas temperatures of species or molecules but not as useful for n_e or T_e measurements [1], [9].

Optical emission spectroscopy (OES) is an established diagnostic that does not require extensive equipment, and line ratio techniques can determine n_e and T_e . However, there is more uncertainty in the measured quantities due to the inexact determination of spectral peaks [9]. With the available resources and predicted plasma operating regime, OES was selected as the main diagnostic tool.

1) *ICCD Camera/Spectrograph Assembly*: PI-MAX from Princeton Instruments is a fiber-optic coupled, ICCD camera (512×512 pixels) capable of a 4-ns gate. The quantum efficiency cutoff for the photocathode and P43 phosphor coating on the PI-MAX intensifier limited the measurable plasma light wavelength to 350–750 nm [13].

Mounted behind the ICCD detector is an Acton SP-308 triple-grating spectrograph. It has a focal length of 0.300 m, an overall spectral range of 185–1100 nm, a resolution of 0.1 nm at 435.8 nm, and an accuracy of ± 0.2 nm. All emission spectra were taken with a 600 gpm (grooves per millimeter) diffraction grating blazed at 500 nm. The slit width of the SP-308 was set to $50 \mu\text{m}$. The light collection volume was approximately 240 mm^3 .

The ICCD-spectrograph assembly is shown in Fig. 3, and both the camera and spectrometer were fully controlled by the WinSpec software. The assembly measured the full emission spectra of a given plasma averaged over 4 ns. At the same plasma conditions, the ICCD trigger was incrementally delayed to capture the full spectra at a given time t later. This will be further discussed in Section II-B. For every emission spectra, a line ratio analysis with spectral modeling software was conducted to determine n_e and T_e at that given instant in time. Doing this analysis over the entire plasma turn-on to turn-off duration provided the time-resolved electron temperature and density for a given set of operational parameters.

For data collection, 20 scans of the plasma emission spectra were taken with a 4-ns gate at each given instant in time for each operating condition and averaged. For higher intensity counts and a lower signal-to-noise ratio, the ICCD was set to 20 gates/spectra.

2) *Calibration*: The spectrometer was wavelength calibrated with an Ocean Optics HG-1 Mercury-Argon light source to obtain the wavelength correction factor that related the spectrometer-measured wavelength to the NIST-determined wavelengths. An intensity calibration was

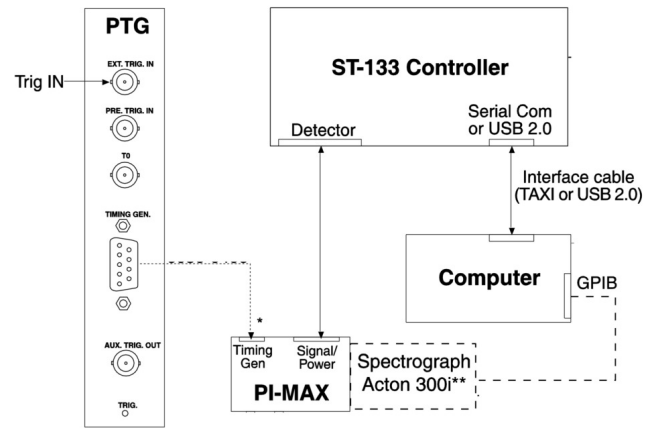


Fig. 3. Schematic of PI-MAX camera connected with an Acton SP-300i spectrograph for OES; adapted from PI-MAX manual [13].

performed with a StellarNet SL1-CAL 2800-K tungsten lamp to obtain the intensity transfer function that related the spectrometer-measured intensity to the StellarNet-provided calibration intensity values.

Due to limitations in the SP-308 field of view, a built-in stitching function (“Step and Glue”) was used. The step and glue data collection range was from 250 to 900 nm with a 10-nm overlap. The final glued spectra were comprised of 13 individual exposures.

3) *Photodiode*: A 400-MHz, low-light capable, ultralow noise avalanche photodiode (ThorLabs APD430A2) was used to track the optical emission output over the lifetime of the plasma. Schwirzke *et al.* used a fast photodiode to measure the delay between the initiation of a voltage waveform and the formation of pulsed plasma [14], and Chan and Singletary used the APD430A2 photodiode in similar experimental setups to investigate the pulse repetition rate on plasma rise time for a nanosecond-pulsed argon plasma [15], [16]. This article utilized the photodiode trace as verification that the generated pulsed plasma was repeatable. Like spectral emission lines, photodiode traces were tracked over several lifetimes of the pulsed plasma. Differences in traces provided qualitative information about how the plasma changed with each pulse.

4) *Optical Setup*: As seen in Fig. 1, an N-BK7 plano-convex lens ($\varnothing 75.0 \text{ mm}$, $f = 85.0 \text{ mm}$) was placed between the plasma cell and the camera–spectrometer assembly to gather and focus a greater amount of emitted light into the spectrometer to ensure spectral peaks could be clearly distinguished at a 4-ns gate. Optical rails and carriages were used for precise alignment of the plasma cell, lens, ICCD-spectrometer assembly, and photodiodes. Spectral intensity was further boosted by commanding the camera to take 20 spectra for every desired delay time, to gate 20 times/exposure, and to set a region of interest (ROI) instead of using the full 512×512 CCD array on the PI-MAX.

To verify the assumption that the ICCD-spectrometer assembly was capturing the same plasma with every gate, a series of tests at different operating conditions was conducted. The NSP voltage waveform, PI-MAX gate

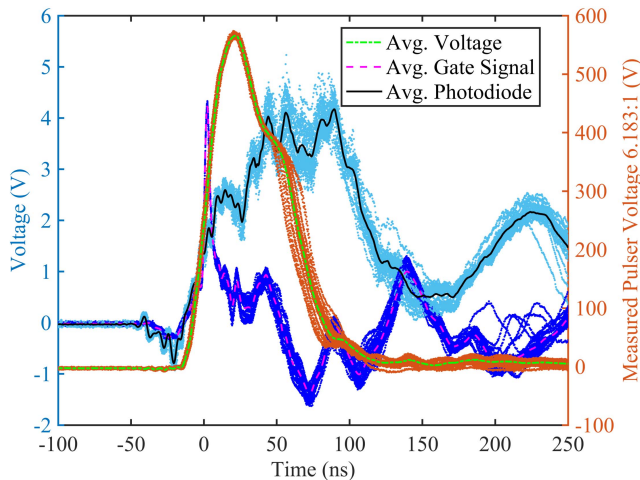


Fig. 4. Measured voltage waveform, photodiode, and 4-ns camera gate monitoring signal over 34 gates with their respective averaged values.

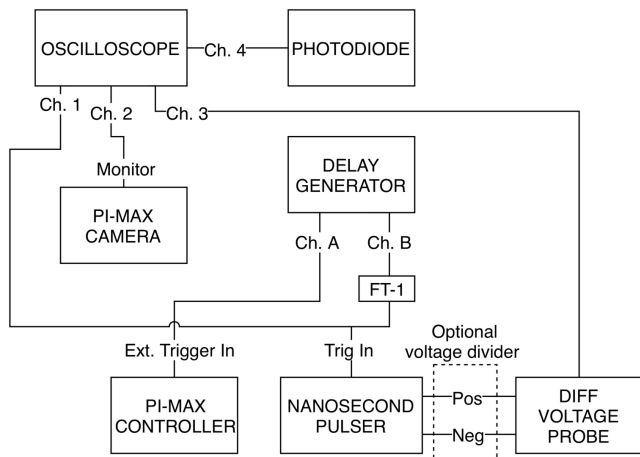


Fig. 5. Timing synchronization setup.

monitoring signal, and photodiode signal were monitored by the oscilloscope. Fig. 4 shows the results of a test where 20 exposures, each with 20 gates/exposure was taken for a 16-kV, 4-kHz plasma at 1 Torr. While the oscilloscope was only fast enough to capture 34 of the 400 gates, Fig. 4 indicates that the measured voltage pulse, plasma light emission as measured by the photodiode, and 4-ns gate window were all consistent and repeatable. Thus, it was reasonable to assume that the voltage waveform was consistent from pulse to pulse and that the camera gated at the same time window for every pulse. It was also reasonable to assume that the plasma, as analyzed by total light emission intensity, was the same for every voltage pulse and spectral shot.

B. Timing Synchronization

Fig. 5 shows the timing setup used to synchronize the pulser, ICCD-spectrometer assembly, and photodiode. A Berkeley Nucleonics Corporation Model 577 pulse delay generator was used as the master clock. A representative timing diagram is shown in Fig. 6. A 500-ns pulse was sent to trigger the NSP as soon as the delay generator began running. The NSP continuously pulsed at T_0 set by the delay generator. Another 300-ns pulse was sent to trigger the PI-MAX camera with a

time delay t_{delay} from the NSP trigger pulse. There was an inherent, constant PI-MAX time offset before the 4-ns gating signal was triggered. By forcing both the pulser and the camera to trigger off the same master clock, t_{delay} could sweep across the voltage pulse to capture light emissions at different parts of the plasma evolution and thus collect time-resolved data of the plasma independent of the NSP.

The pulse from the delay generator to externally trigger the NSP was received by the Eagle Harbor Fiber Transmitter (FT-1), which had a fiber-optic output and a 50 Ω -terminated BNC input that required a smooth, 5-V input trigger signal provided by the Model 577 [17]. The NSP's pulse frequency was controlled by the pulse generator, but the pulsewidth and voltage discharge were manually set on the NSP front panel by the user.

The delay between the trigger pulse and the actual start of the high-voltage pulse was consistently measured to be ≈ 30 ns. Specific time delays due to cable lengths were not explicitly calculated, but those delays were incorporated in determining the initial t_{delay} for each operating condition.

C. Voltage Measurements

Pulser discharge voltage was measured with a Teledyne Lecroy HVD3605A high-voltage differential probe connected to a Teledyne Lecroy HDO6104A oscilloscope. Voltages greater than the 6-kV maximum for the differential probe were used, so a resistive voltage divider was implemented. Adapted from [18], the divider consisted of $5 \times 1000 \Omega$ HVR RT series resistors. With the NSP internal series resistance of 1170 Ω , a single resistor gave a nominal voltage division of 1:6.183.

1) *Mitigating Voltage Reflections*: To minimize stray capacitive coupling and therefore ringing and noise prevalent for high-voltage pulses for accurate voltage measurements, the power leads, voltage divider, and probes were lifted off the metal optical table by at least 6 in. The NSP output cable length was 70 in long, so the propagation time of a signal through the cable (≈ 5.8 ns) was short compared to the signal's rise time (measured average of ≈ 24.6 ns), and all diagnostics and leads were laid out, so no cables crossed or looped around each other. The resulting voltage waveform shown in Fig. 7 was deemed clean enough for testing. Due to the high voltage and short pulsewidth, the rise and fall times of the pulser dominated, and the 20 ns was the "steady-state" portion of the pulse.

III. SPECTRAL ANALYSIS

To translate spectral measurements into time-resolved plasma properties, the plasma population densities needed to be calculated with a valid model. This section discusses the validity conditions of the four plasma equilibrium models and explains how an intensity line ratio analysis coupled with a collisional-radiative simulation software was used to calculate the experimental T_e and n_e .

A. Equilibrium Plasma Models

There are a number of elementary processes that change the distribution of atoms and ions in a given energy state. A selection of processes for an argon plasma is detailed below.

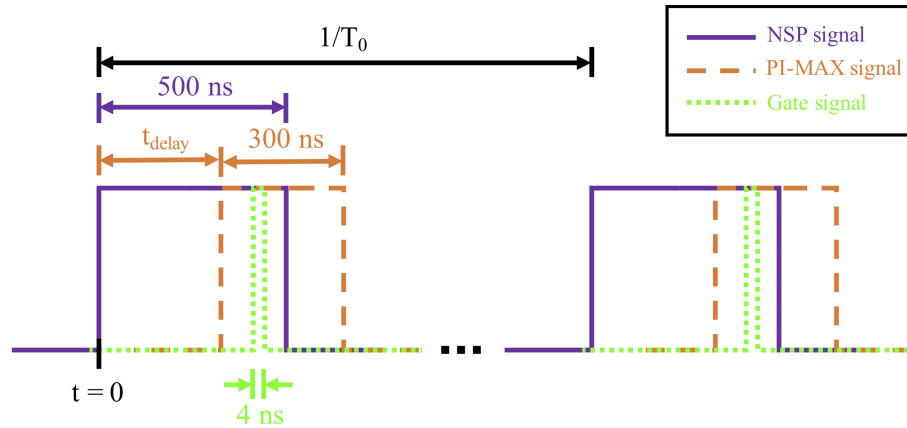


Fig. 6. Timing relationship of the delay generator, pulser, and PI-MAX-SP-308 assembly.

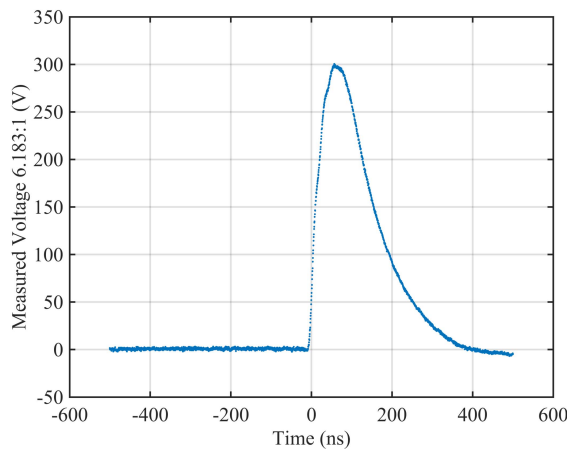
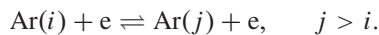
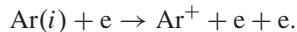


Fig. 7. NSP voltage measurement with 6.183:1 resistive voltage divider. NSP set to 2 kV, 20 ns.

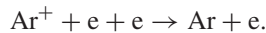
- 1) Electron-impact (collisional) excitation and de-excitation:



- 2) Electron-impact (collisional) ionization:



- 3) Three-body recombination:



- 4) Photoionization and radiative recombination:



- 5) Photoexcitation and spontaneous/stimulated emission:



Using local thermal equilibrium (LTE) validity conditions, Griem proposed a widely accepted criterion later modified by Numano to give the LTE critical electron number density in cm^{-3} [19]–[21]:

$$n_e^* \approx 9.3 \times 10^{17} \left(\frac{E_{12}}{E_1^H} \right) \left(\frac{E_1^H}{kT_e} \right)^{1/2} \quad (1)$$

where E_{12} is the ionization energy of a given atom from the ground state to the first ionized state in eV and E_1^H is the first ionization energy of hydrogen in electronvolt.

Based on previous work with similar plasmas, the electron density is expected to be several orders of magnitude too low for LTE, but higher than what is typically valid to use the coronal approximation ($10^{10}/\text{cm}^3$) [16], [20], [22]. Therefore, a collisional-radiative model (CRM) was used to calculate the theoretical spectral line intensities.

B. Collisional-Radiative Model

In CRMs, densities of excited states are purely determined by collisional and radiative processes and balanced rate equations [23]. No specific equilibrium needs to be assumed, but most CRMs assume a Maxwellian electron velocity distribution [22]–[25].

CRMs solve coupled differential equations that describe densities of an excited state j in the plasma with collisional and radiative processes and calculate n_e and T_e [23]:

$$\frac{\partial n(j)}{\partial t} + \nabla \cdot (n(j)\omega_p) = \left(\frac{\partial n(j)}{\partial t} \right)_{c,r}. \quad (2)$$

All changes in excited-state population density due to collisional (c) and radiative (r) processes are encompassed on the right-hand side of the equation. More detailed discussions and reviews of CRMs and the major collisional and radiative processes for different argon excited states are found in literature [19], [22]–[30].

C. Line Ratio Analysis

n_e can be directly determined from peaks of the OES-measured spectra. However, the accuracy of this method is highly dependent on how well a given fit profile (i.e., Gaussian, Lorentzian, single-Voigt, etc.) matches the data profile for a peak [9], [31]. Linewidth broadening effects such as Stark broadening [19], [26], [27], [32], [33], Doppler broadening [34], instrumental broadening [35], van der Waals, and resonance broadenings [31] need to be considered and included in the fit.

An alternative analysis for n_e and T_e is to take ratios of spectral line intensities. This method removes the difficult task of accurately determining line-broadening parameters and only involves intensity ratios of different wavelengths. Calculated n_e and T_e values from the line ratio analysis have been similar to those calculated directly from a spectral line fit [26], [27].

Under CTE or LTE, the intensity ratio between two spectral lines, usually chosen to have the same lower level, directly gives plasma electron temperature [5], [36]:

$$\frac{I_1}{I_2} = \frac{A_1 g_1 \lambda_2}{A_2 g_2 \lambda_1} \exp\left(-\frac{E_1 - E_2}{kT_e}\right) \quad (3)$$

where I is the relative or absolute intensity from an emission spectral line, A is the tabulated Einstein coefficient (transition probability), g is the tabulated multiplicity, and E is the energy associated with the upper energy level. Relative intensity is typically used to avoid a lengthy absolute calibration.

Rearranging 3 gives

$$\ln \frac{I_1 A_2 g_2 \lambda_1}{I_2 A_1 g_1 \lambda_2} = -\frac{1}{kT_e} (E_1 - E_2). \quad (4)$$

The slope of the semilog plot of 4 is $-\Delta E/T_e$. Electron temperature can, therefore, be directly calculated from the experimental spectral lines using the Boltzmann relations if the plasma is in CTE or LTE [37]. If the plasma is in partial LTE or is in nonequilibrium, the correction factors or a different model like a CRM must be used. From a CRM, theoretical spectral line intensities can be calculated, and the measured spectral intensity line ratios can be matched to calculated line ratios to determine the experimental n_e and T_e [24].

Using 1 and $E_{12} = 15.76$ eV for argon, $n_e^* \approx \mathcal{O}(10^{19}) \text{ cm}^{-3}$ for LTE to be valid. Based on similar plasmas in literature, the experimental electron density was predicted to be $\mathcal{O}(10^{10} - 10^{12}) \text{ cm}^{-3} \ll n_e^*$. LTE thus did not apply to this plasma, but n_e was too high for the coronal model, so CRM was used. For this article, the intensity ratio of emission lines from the ICCD-spectrometer measurements were matched to results generated from the collisional-radiative simulation software PrismSPECT.

D. PrismSPECT

PrismSPECT is a commercial software that uses a CRM and user-based inputs such as gas mixture, background gas pressure, plasma geometry, and electron temperature to generate theoretical emission spectra for LTE and non-LTE plasmas. For the theoretical argon emission spectra, PrismSPECT takes into account collisional ionization, recombination, excitation and de-excitation, photoionization and stimulated recombination, photoexcitation and stimulated emission, spontaneous decay, radiative recombination, autoionization, and electron capture [38]. Electron density as a function of electron temperature and background gas pressure is directly calculated by PrismSPECT using a CRM.

A zero-width, optically thin, non-LTE plasma was assumed. As suggested in literature, simulations used a single-temperature Maxwellian electron distribution [20], [24]. The density model was calculated by fixing an argon pressure in the plasma cell, assuming the ideal gas law, and allowing the

gas temperature to respond within the set volume of the plasma cell. Low-temperature spectroscopy was used as the modeling mode as the other spectral modes were more suitable for hot plasmas such as those seen in fusion reactor experiments. Results from each simulation included the generated emission spectra, ion population, and line intensities for user-selected wavelengths.

IV. RESULTS AND DISCUSSION

This section details the nanosecond-pulsed plasma tests that were conducted and the OES line ratio analysis coupled with the PrismSPECT collisional-radiative software to obtain electron temperature and electron density. Trends in the time evolution of electron temperature and electron density at various operating conditions were discussed, as well as the uncertainties associated with the results.

A. Test Matrix

Pressure (1–3 Torr), discharge voltage (8–20 kV), and pulser repetition frequency (0.5–8 kHz) were the main experimental parameters modified to investigate their effects on plasma properties. An example test matrix for a frequency study at 1 Torr, 8 kV would be to set pulser frequency at 0.5, 1, 2, 4, and 8 kHz. At each test operating condition, the delay times were swept from the onset of a photodiode signal to ~ 20 ns past the end of the voltage pulse unless otherwise noted. The delay time difference between two consecutive gates was 2 ns for the first 80% of the sweep and 4 ns for the last 20%.

B. NSP Voltage Waveforms

Fig. 8 shows the sample waveforms from the six discharge voltage conditions that were used for nanosecond-pulsed plasma testing. Each set of discharge voltage waveform corresponded to 60–74 gates. While the rise time of all sets of voltage waveforms were consistent, the fall times were dependent on the voltage. Lower voltages (8 and 10 kV) had longer fall times. The 14-kV condition was the bounding case. Table I lists the desired NSP voltage, actual outputted voltage, and rise and fall times of the voltage pulse, defined as the interval between 10% and 90% of the peak amplitude [5].

The long RC time decay at lower voltages could be because the energy going into the plasma cell load first charged the capacitance of the load and then drained through the NSP's internal resistors after the pulse. At higher voltages, the energy went directly into the plasma or was high enough that it caused a breakdown in the capacitance of the load. This could explain why the 14-kV condition seemed to generate the most visually "unstable" and flickering plasma. This discharge voltage was just high enough that some voltage pulses were going directly into the plasma while others were charging and discharging the plasma cell capacitance. This can be seen in Fig. 8 where the voltage decay of the 14-kV condition was distinctly separated into a fast and a slow decay. Note that increasing the discharge voltage brought fall times closer to the rise times, potentially because the capacitive discharge did not occur.

The voltage seen by the plasma cell load was not the same as what was requested from the NSP because of the

TABLE I
VOLTAGE WAVEFORM PROPERTIES FOR NANOSECOND-PULSED PLASMA GENERATION

Discharge Voltage (kV)	Measured Voltage (kV)	% Difference	Rise Time (ns)	Fall Time (ns)
8	2.20	72.5%	27.6	306.0
10	2.73	72.7%	26.0	169.2
12	2.99	75.1%	24.8	98.8
14	3.31	76.4%	23.6	80.4
16	3.68	77%	22.8	43.2
20	4.37	78.1%	22.8	38.0

TABLE II
SELECTED ARGON NEUTRAL SPECTRAL LINES FOR LINE RATIO CALCULATIONS OF NANOSECOND-PULSED PLASMA

Ar I Air Wavelength (nm)	Rel. Intensity	Transition	A_{ki} (s^{-1})	Energy Levels (eV) [39]
696.5431	10000	$4p^2[1/2]1 \rightarrow 4s^2[3/2]2$	6.40×10^6	11.5484 \rightarrow 13.3279
706.7218	10000	$4p^2[3/2]2 \rightarrow 4s^2[3/2]2$	3.80×10^6	11.5484 \rightarrow 13.3022
727.2936	2000	$4p^2[1/2]1 \rightarrow 4s^2[3/2]1$	1.83×10^6	11.6236 \rightarrow 13.3279
738.3980	10000	$4p^2[3/2]2 \rightarrow 4s^2[3/2]1$	8.50×10^6	11.6236 \rightarrow 13.3022
750.3869	20000	$4p^2[1/2]0 \rightarrow 4s^2[1/2]1$	4.50×10^7	11.8281 \rightarrow 13.4799

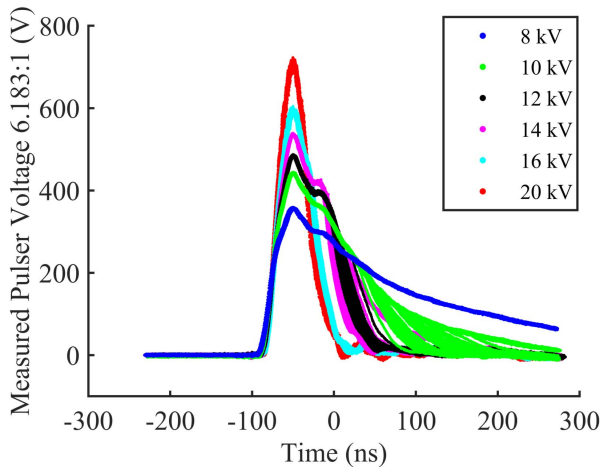


Fig. 8. Comparison of low-voltage and high-voltage pulses on the NSP.

short 20-ns pulsewidth and the resistive plasma cell load. However, there was a proportional difference in the desired output to measured voltage, so meaningful trends could still be observed. Similarly, although the voltage pulse was set to 20 ns, the NSP only reached steady state for 5–8 ns, which was enough for 1–2 emission spectra to be captured, so changes in plasma behavior could still be established with these voltage pulses.

C. OES Analysis Overview

The Ar I and Ar II lines selected for line ratio calculations are listed, respectively, in Tables II and III. Lines within the PI-MAX wavelength range and at least 2 nm away from other argon neutral and ion +1 peaks in the NIST database were chosen to minimize any peak matching errors. The transitions for each wavelength, transition probabilities (A_{ki}), and energy levels ($E_i \rightarrow E_k$) for the transitions are given as reference

from [39]. Transitions are written as electron configuration, term, and angular momentum J , and energy levels are given to four decimal places.

Three PrismSPECT simulations were run, one at each test pressure of 1, 2, and 3-Torr argon. Each pressure simulation had a different electron temperature range, but all ran with a resolution of 0.005 eV.

Images of the plasma (taken with a Nikon D90 at $f/18$ aperture and 1/30 shutter speed) are shown in Figs. 9–11. As discharge voltage and pulse frequency increased, the plasma became brighter, as demonstrated by the increased maximum intensities in the emission spectra (Fig. 12). As pressure increased, the plasma column between the two electrodes visibly narrowed. At 1-Torr argon, the plasma looked like a glow discharge around the positive (bottom) electrode. At 2 Torr, the plasma started to bridge the gap to the negative electrode in a funnel shape. By 3 Torr, the plasma had formed a narrow and focused beam across the two electrodes. As seen in Fig. 12, the wavelengths of the emission spectra corresponding to excited argon neutrals and argon +1 ions had a large boost in intensity as pressure increased due to the additional atoms available for excitation and ionization.

D. Line Ratio Comparison

At each time delay, wavelengths in Tables II and III were used for line ratio calculations. Each Ar II wavelength peak in a given emission spectrum was compared to each Ar I line. Each experimentally determined T_e and n_e from line ratios was averaged to calculate a representative T_e and n_e at a time delay for an operating condition.

The range of electron temperatures (1–2 eV) and densities ($10^{14} - 10^{15} \text{ cm}^{-3}$) from all line ratio calculations at different operating conditions corresponded well to experimentally determined and modeled values of similar plasmas in literature [24], [26], [27], [40].

TABLE III
SELECTED ARGON ION +1 EMISSION SPECTRAL LINES FOR LINE RATIO CALCULATIONS OF NANOSECOND-PULSED PLASMA

Ar II Air Wavelength (nm)	Rel. Intensity	Transition	A_{ki} (s^{-1})	Energy Levels (eV) [39]
404.2893	288	$4p^2D\ 3/2 \rightarrow 4s^2D\ 3/2$	4.06×10^7	18.4265 \rightarrow 21.4924
407.2004	708	$4p^2D\ 5/2 \rightarrow 4s^2D\ 5/2$	5.80×10^7	18.4541 \rightarrow 21.4980
413.1723	891	$4p^2P\ 1/2 \rightarrow 4s^2D\ 3/2$	8.50×10^7	18.4265 \rightarrow 21.4265
427.7528	1995	$4p^2P\ 3/2 \rightarrow 4s^4P\ 3/2$	8.00×10^7	18.4541 \rightarrow 21.3518
434.8064	1995	$4p^4D\ 7/2 \rightarrow 4s^4P\ 5/2$	1.17×10^8	16.6439 \rightarrow 19.4945
440.0986	8710	$4p^4P\ 5/2 \rightarrow 3d^4D\ 7/2$	3.04×10^7	16.4065 \rightarrow 19.2229
442.6001	1514	$4p^4D\ 5/2 \rightarrow 4s^4P\ 3/2$	8.17×10^7	16.7485 \rightarrow 19.5490
454.5052	1738	$4p^2P\ 3/2 \rightarrow 4s^2P\ 3/2$	4.71×10^7	17.1400 \rightarrow 19.8672
460.9567	2291	$4p^2F\ 7/2 \rightarrow 4s^2D\ 5/2$	7.89×10^7	18.4541 \rightarrow 21.1431
465.7901	1445	$4p^2P\ 1/2 \rightarrow 4s^2P\ 3/2$	8.92×10^7	17.1400 \rightarrow 19.8011
472.6868	23442	$4p^2D\ 3/2 \rightarrow 4s^2P\ 3/2$	5.88×10^7	17.1400 \rightarrow 19.7623
476.4864	2344	$4p^2P\ 3/2 \rightarrow 4s^2P\ 1/2$	6.40×10^7	17.2658 \rightarrow 19.8672
480.6020	1820	$4p^4P\ 5/2 \rightarrow 4s^4P\ 5/2$	7.80×10^7	16.6439 \rightarrow 19.2229
487.9863	2239	$4p^2D\ 5/2 \rightarrow 4s^2P\ 3/2$	8.23×10^7	17.1400 \rightarrow 19.6800
501.7163	7413	$4p^2F\ 5/2 \rightarrow 3d^2D\ 3/2$	2.07×10^7	18.6565 \rightarrow 21.1270

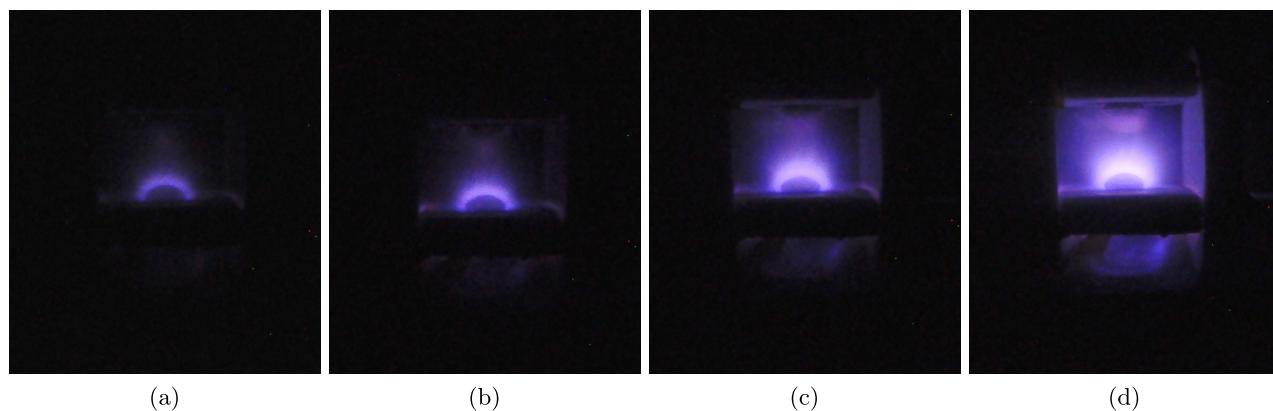


Fig. 9. Nanosecond-pulsed plasma at different pulse frequencies, 10 kV, and 1 Torr. (a) 1 kHz. (b) 2 kHz. (c) 4 kHz. (d) 8 kHz.

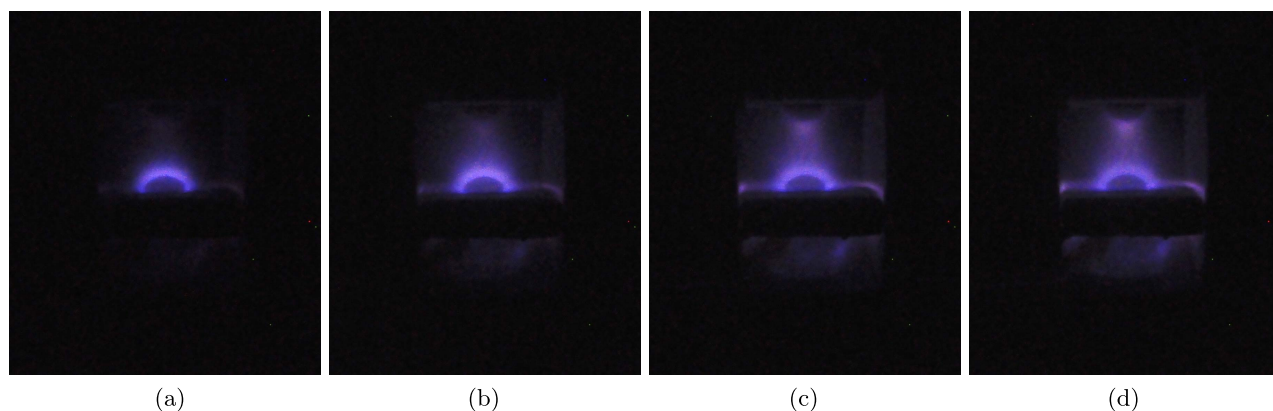


Fig. 10. Nanosecond-pulsed plasma at different discharge voltages, 2 kHz, and 1 Torr. (a) 8 kV. (b) 12 kV. (c) 16 kV. (d) 20 kV.

Figs. 13–17 show the time-resolved electron temperature and electron density of the nanosecond-pulsed plasmas generated with selected operating conditions to demonstrate trends in plasma behavior. Representative error bars were shown on every 5th data point to prevent over-cluttering the plots. The x -axis spans from 5% of the maximum voltage pulse on the rising edge to 15% of the maximum photodiode signal on the falling edge or to the last test taken for the lower voltage (i.e. 8 and 10 kV), lower pulse repetition (i.e. 0.5 and 1 kHz)

conditions. Time at 0 is defined as the time of the maximum voltage pulse to normalize the different tests.

E. Effects on Electron Temperature

As pulse frequency increased, the value of maximum T_e was larger, and the time of that maximum T_e shifted leftwards in time (i.e., T_e rose and decayed faster in time). For example, in Fig. 13, the 500-Hz case took almost 40 ns past the peak

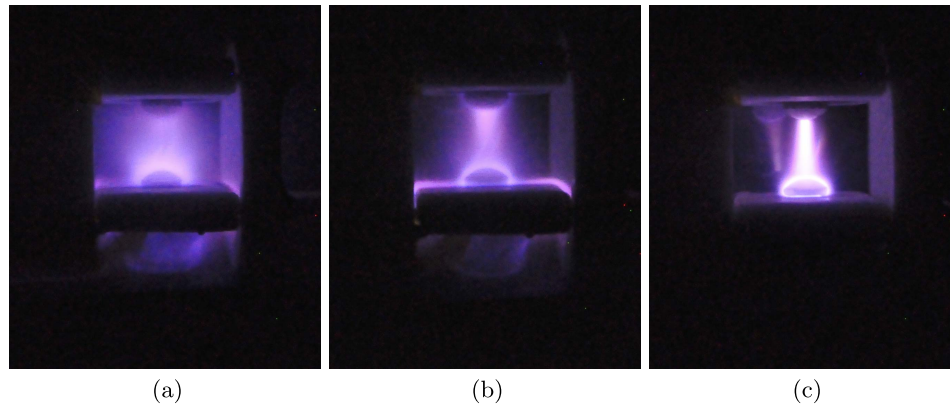


Fig. 11. Nanosecond-pulsed plasma at different pressure conditions, 20 kV, and 4 kHz. (a) 1 Torr. (b) 2 Torr. (c) 3 Torr.

voltage pulse to reach maximum T_e , while the 8-kHz case reached maximum T_e about 35 ns before peak voltage. This indicates that a large distinction in the plasma dynamics of high- and low-frequency pulsed plasmas is how the intensities of argon neutrals and ions rise and fall. Line ratio was defined as neutral intensity to ion intensity, so higher ion counts with a similar neutral count gave a lower line ratio and thus a higher T_e . At lower frequency plasmas, Ar I dominated the emission spectra. Both Ar I and Ar II initially increased as delay time was increased. However, Ar I counts were initially 2–3 times larger than Ar II counts, so more argon neutrals were ionized and the Ar II counts increased, the line ratio dropped, and T_e thus increased with time. Eventually, Ar II counts began to decrease, while Ar I counts increased, and T_e dropped.

For high-frequency plasmas (i.e., 4 and 8 kHz), T_e started close to a maximum value because ion emission was stronger than neutral emission at the low voltage. With time (as the voltage pulse increased), more neutrals were excited, thus continuously increasing the intensity of Ar I and decreasing T_e . No rise was seen in these high-frequency plasmas, potentially because the ICCD/spectrometer was not sensitive enough. A low T_e (< 1 eV) required Ar II counts 100–1000-s times smaller than Ar I counts. These extremely low intensities occurred before 5% maximum voltage pulse where the spectral signal-to-noise ratio was ~ 1 and was therefore too low to calculate an accurate line ratio.

While electron temperature varied temporally for the voltage studies, similar to the pulse frequency studies, the maximum T_e was only weakly dependent, if not independent, on the applied voltage. Electron temperature decayed faster with increasing discharge voltage, similar to simulation results observed by Liu *et al.* [40]. Lower voltages, such as the 8-kV case in Fig. 14, gave a more steady T_e output for longer, which was directly correlated with the longer voltage pulse fall times of lower voltages shown in Table I. However, conducting the voltage study at a high pulse frequency like 4 kHz in Fig. 15 demonstrated that all voltages, even lower discharge voltages, reached their maximum T_e before maximum voltage. This was additional evidence that increasing pulse frequency shifted maximum electron temperature leftwards in time.

The pressure effect on electron temperature was the least obvious. All plasmas in the pressure study groups had a rise

and decay in electron temperature, but the different pressures time-shifted these events such that higher-pressure plasmas reached maximum T_e and began decaying soonest in time. There was also a trend of electron temperature being inversely proportional to pressure, which correlated with results from literature [41]. There was a shorter mean free path at the increased pressure conditions. The resulting, more frequent collisions led to greater thermal energy loss and therefore a lower T_e as well as increased energy transfer and therefore higher T_e rise and decay rates.

Note that the maximum T_e and n_e for the 3-Torr test conditions are not seen in the resulted figures (Figs. 16 and 17) as they occurred before 5% maximum voltage. With a high starting density of argon neutrals, a small discharge voltage could create a high argon ion density and intensity and therefore a maximal T_e .

F. Effects on Electron Density

While the maximum electron density of a plasma was relatively independent of pulse frequency, higher frequencies started at a lower n_e at a given time and had a faster decay rate. The visual results in Fig. 9 show that a significantly brighter plasma was generated as pulser frequency was increased, but an independence in n_e from the time-resolved results indicated that while higher pulser frequencies introduced more electrons to the plasma system, more argon neutrals were not ionized. Instead, the dominant process and the cause of the increased visual intensity in the plasma was a large increase in excited argon neutral population. The faster n_e decay rate at higher pulse frequencies could be a result of more three-body recombination processes occurring as more electrons were pushed through the plasma more often.

The electron density profile was also relatively invariant with respect to voltage, but higher discharge voltage conditions led to n_e decaying sooner after maximum voltage pulse, similar to the T_e response. Therefore, changing discharge voltage changed how soon recombination processes occurred in the plasma, with higher voltage plasmas recombining sooner. The n_e decay rates were approximately constant across the voltage cases.

In general, for the 1-Torr cases, maximum n_e was temporally later than maximum voltage pulse. This time delay

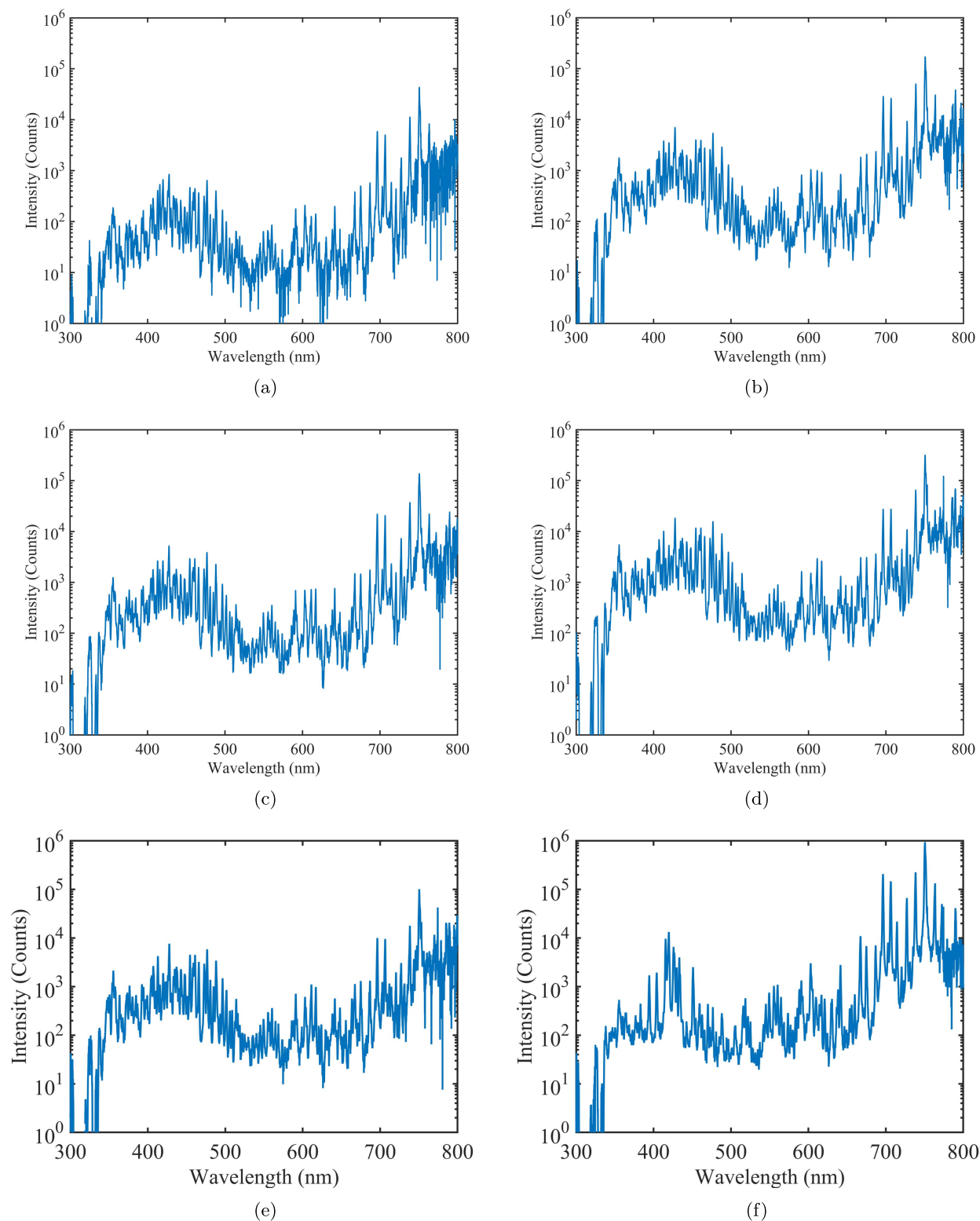


Fig. 12. Emission spectra of nanosecond-pulsed plasma at different operating conditions. (a) and (b) Increasing discharge voltage. (c) and (d) Increasing pulser frequency. (e) and (f) Increasing pressure. All spectra shown were taken at the gate time corresponding to maximum voltage pulse. (a) 1 Torr, 8 kV, 1 kHz. (b) 1 Torr, 20 kV, 1 kHz. (c) 1 Torr, 16 kV, 1 kHz. (d) 1 Torr, 16 kV, 4 kHz. (e) 1 Torr, 10 kV, 4 kHz. (f) 3 Torr, 10 kV, 4 kHz.

could be attributed to the dependence of ionization rate to electron temperature. The argon neutral and ion population fraction at a given pressure from PrismSPECT was used as an indicator of ionization rate (i.e., higher populations of a given

ion imply higher ionization rate for that ion). The crossover between argon neutral and +1 ions at 1 Torr is 1.15 eV (shown in Fig. 18), and n_e for Figs. 13-15 began to decay when $T_e \approx 1.25 - 1.35$ eV.

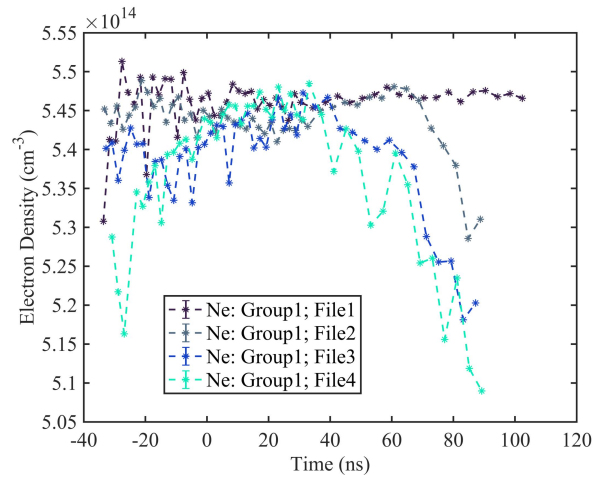
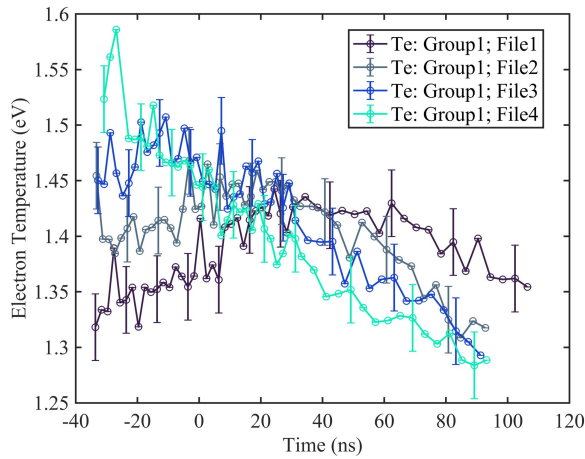


Fig. 13. Time-resolved results of pulse frequency study at 1 Torr, 10 kV.

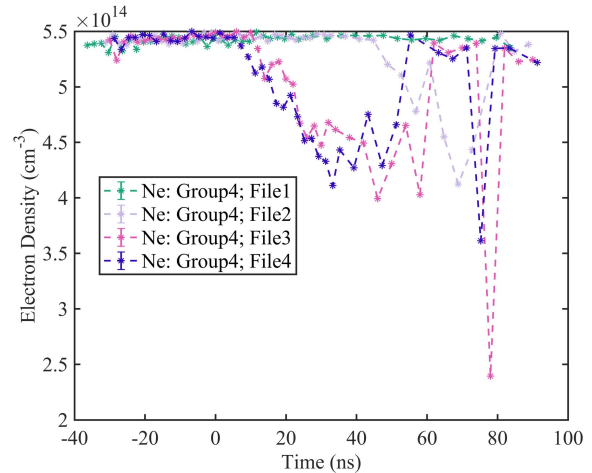
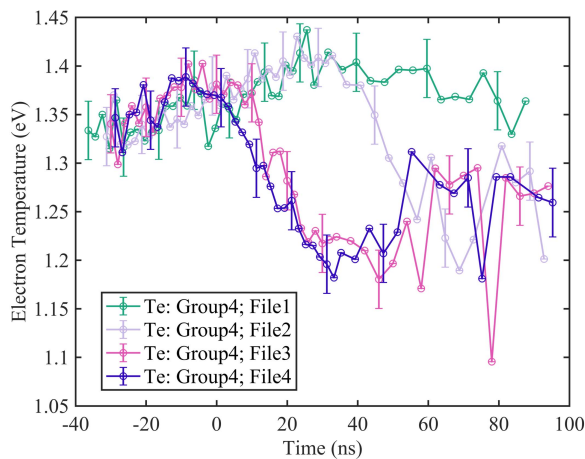


Fig. 14. Time-resolved results of voltage study at 1 Torr, 1 kHz.

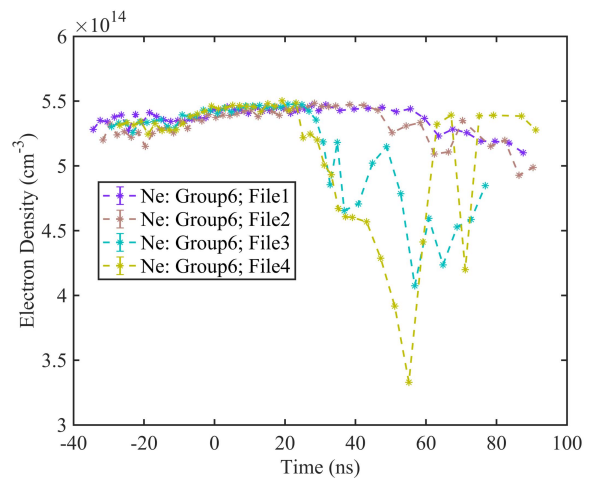
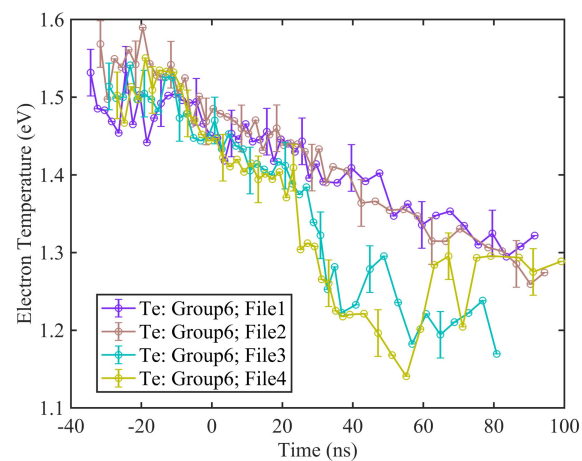


Fig. 15. Time-resolved results of voltage study at 1 Torr, 4 kHz.

The effect of pressure on electron density was approximately linear (Figs. 16 and 17). n_e for all three pressures followed similar but time-shifted temporal profiles. In Fig. 16, where additional tests were taken for the 1-Torr

case past the voltage pulse, n_e displayed the same behavior as the 2-Torr and 3-Torr cases, but the time scales for the constant, drop, rise, and slow decay of n_e were significantly longer. This faster temporal response at higher pressures

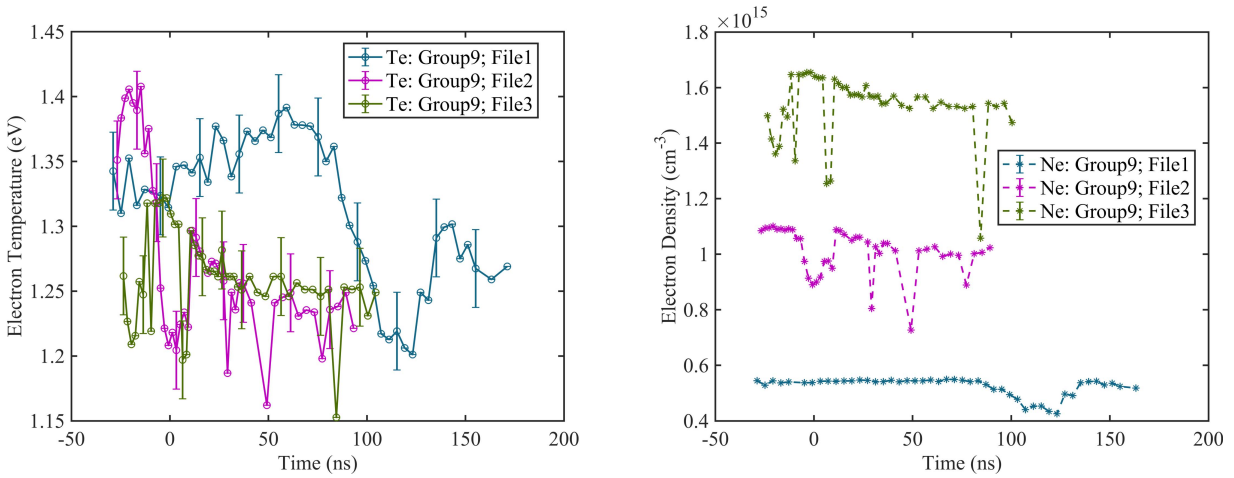


Fig. 16. Time-resolved results of pressure study at 14 kV, 1 kHz.

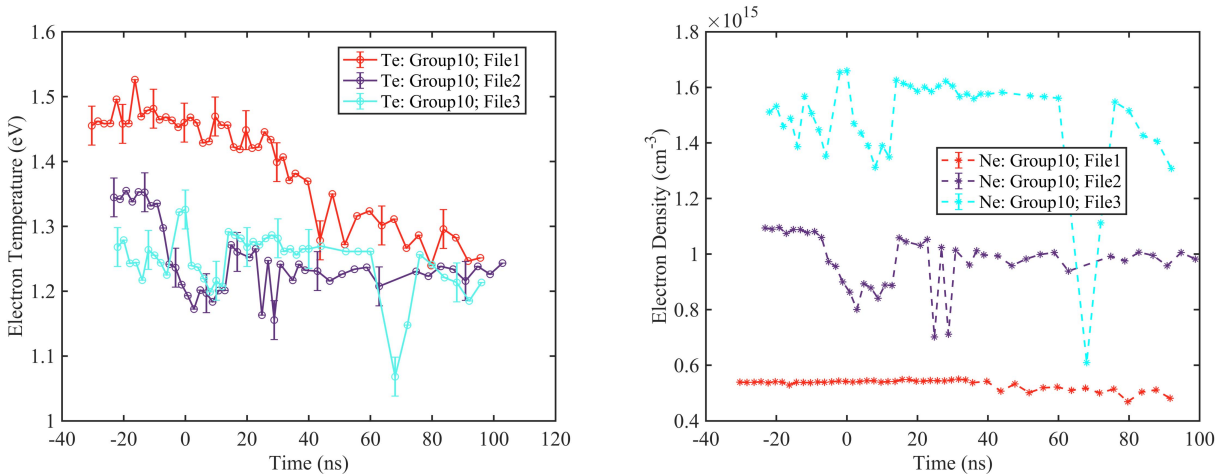


Fig. 17. Time-resolved results of pressure study at 14 kV, 4 kHz.

could be attributed to greater recombination at higher pressures.

G. Ionization and Recombination Times

From the data provided and with reference to PrismSPECT simulations of argon neutral and ion populations, plasmas in all operating conditions had ionization times in the tens of nanoseconds based on the difference in time between the crossover point of Ar I and Ar II populations and the initiation of the voltage pulse. Although longer than ionization times, the plasmas also had recombination times in the tens of nanoseconds (10–100 ns). Higher discharge voltages and higher frequencies led to faster electron density decay, which suggested faster recombination times.

H. Uncertainty Analysis

The time-resolved electron temperature, electron density, and plasma frequency values were obtained from several averaging steps, and this section breaks down the uncertainties involved in data collection and analysis.

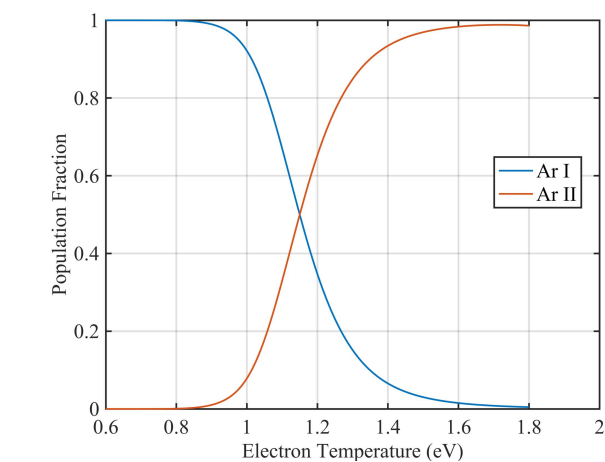


Fig. 18. PrismSPECT-simulated population fraction (normalized to their respective maximum values) of argon neutrals (Ar I) and ions (Ar II) as a function of electron temperature for a 1-Torr plasma.

The camera–spectrometer setup necessitated the collection of emitted light from a spherical volume of the nanosecond-pulsed, argon plasma discharge. This light was collectively

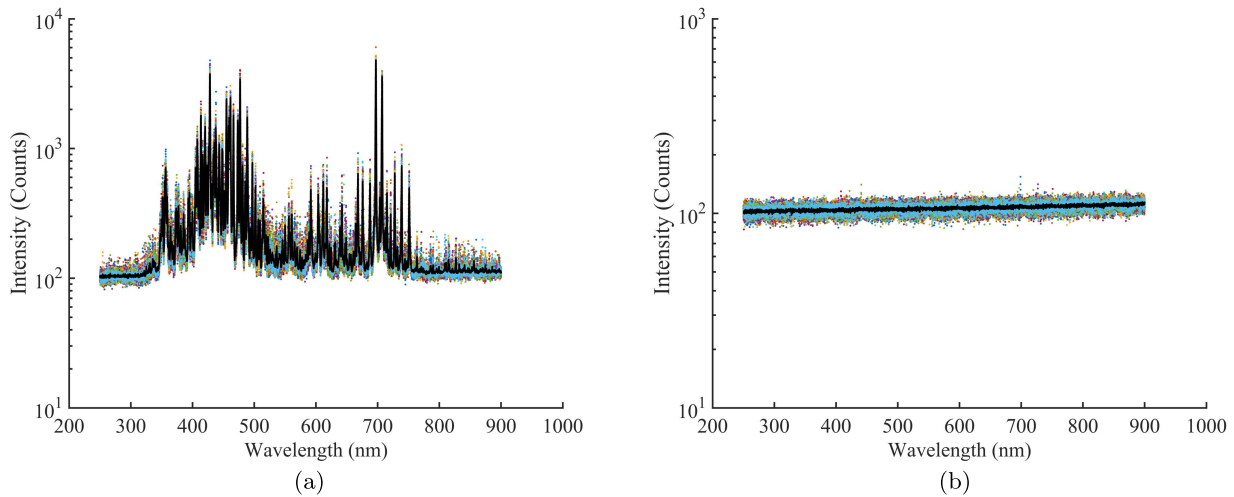


Fig. 19. Twenty individual raw emission spectra at a given delay time and the averaged emission spectra (in black) to demonstrate repeatability and low variation of the individual emission spectra. (a) Light spectra. (b) Dark spectra.

passed into the spectrometer slit as a spatial average. Therefore, the emission spectra contained no information about a specific, spatial location in the plasma but rather of the spatially averaged, volumetric plasma discharge.

While there was uncertainty associated with spatial inhomogeneities and spatial averaging, the averaged emission spectra are representative of the overall plasma, as shown in literature [22], [26], [27], [32], [35]. Accordingly, the spatial-averaged light was sufficient for the results presented herein, which were results for the overall plasma. However, it was important to analyze the uncertainty due to spectral and temporal averaging used in data processing.

The averaged dark-subtracted spectrum was used for the experimentally determined line ratios rather than the raw emission spectra. The average spectrum, representative of all emission spectra at each given time in the plasma's lifetime, was generated by averaging 20 raw light spectra and subtracting the average of 20 raw dark spectra. To investigate the effects of spectra emission averaging, over 10000 different light and dark spectra were analyzed—20 raw emission spectra for 51 time delays of ten randomly chosen test conditions. Fig. 19 shows the example light and dark spectra, each with 20 raw emission spectra and the calculated average spectra. A bound on maximum uncertainties of 12% and 3% were calculated for the average light and dark spectra, respectively, by looking at the worst case differences between the average and raw spectra. The overall uncertainty for spectra averaging is <12%, as calculated with a geometric mean for uncorrelated uncertainties [42].

The other critical averaging step was in the line ratio analysis where the T_e and n_e values corresponding to each Ar I to Ar II intensity line ratio of a given time (as detailed in Tables II and III) were averaged to obtain the time-resolved T_e and n_e . An analysis was conducted to determine bounds on the effect of averaging the emission spectra and line ratios on the final T_e and n_e values. It is important to note that different line ratios have differing sensitivities to T_e and n_e [24]. Therefore, the collective uncertainty was determined

empirically using an analysis that tracked five test conditions through the entire process to calculate the maximal effects averaging would have on T_e and n_e . Results of the tracked process for the 12 kV, 1 kHz, 1 Torr test condition (Group 4 in Fig. 14) are detailed in Fig. 20.

Fig. 20 illustrates the electron temperature and electron number density calculated from the averaged line ratio of each of the 20 individual emission spectra for a given delay time. The error bars represent the standard deviation calculation of individual line ratios for each spectrum. The T_e and n_e values and standard deviation of individual line ratios as calculated from the average emission spectrum (i.e., $1.39 \text{ eV} \pm 0.041 \text{ eV}$ and $5.45 \times 10^{14} \text{ cm}^{-3} \pm 7.80 \times 10^{12} \text{ cm}^{-3}$) are shown as solid red and dotted lines, respectively. The solid red line also represents the values of T_e and n_e used in the time-resolved, nanosecond-pulsed plasma results.

In all tests analyzed, >95% of the electron temperature and number density from all individual spectra were within the standard deviation bounds of the calculated values from the averaged emission spectra. That is, each individual emission spectrum was within the error bound for the average value with a probability $P \geq 0.95$. It was, therefore, justified to use the averaged emission spectra for T_e and n_e line ratio calculations with confidence to within the standard deviation. The averaged result was used to help suppress random errors in this measurement. The maximum uncertainty bound was 11% and 8% for electron temperature and density, respectively.

Another analysis was conducted for the uncertainty bound in line ratio averaging. The T_e and n_e values were calculated for each individual line ratio of a dark-subtracted emission spectrum. Fig. 21 shows the results from a single emission spectrum from the same test condition (12 kV, 1 kHz, 1 Torr) as above. The mean and standard deviation of the electron temperature and density values for individual line ratios were represented by the red solid and red dotted lines, respectively. Greater than 75% of all analyzed T_e line ratio sets and >85% of n_e line ratio sets were within the standard deviation bounds of the averaged line ratio. With a maximum uncertainty

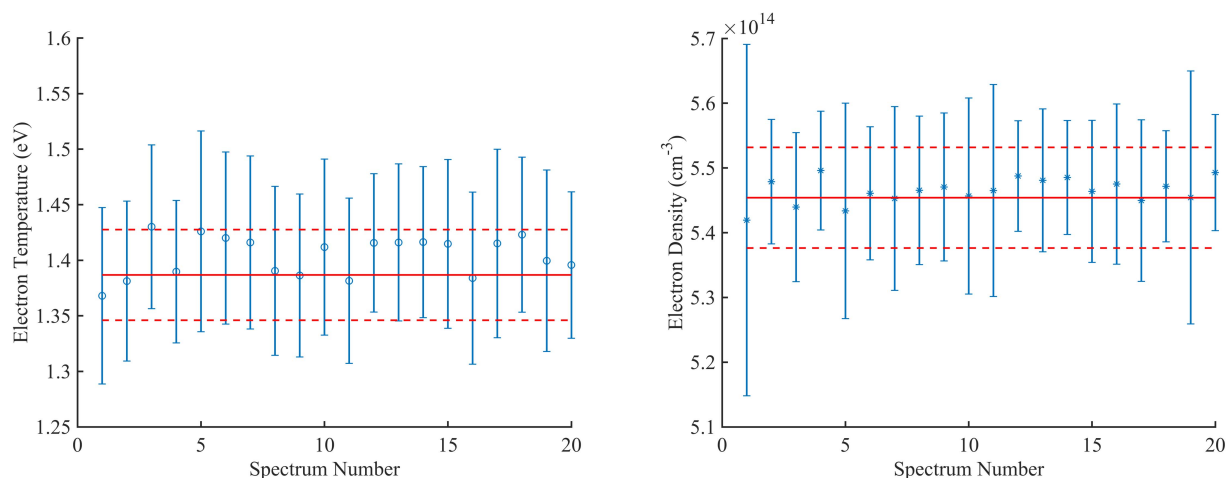


Fig. 20. Spread of 20 T_e and n_e values from each emission spectrum at a given delay time and test condition (blue markers). T_e and n_e values and standard deviation from the averaged spectra (solid and dotted red lines).

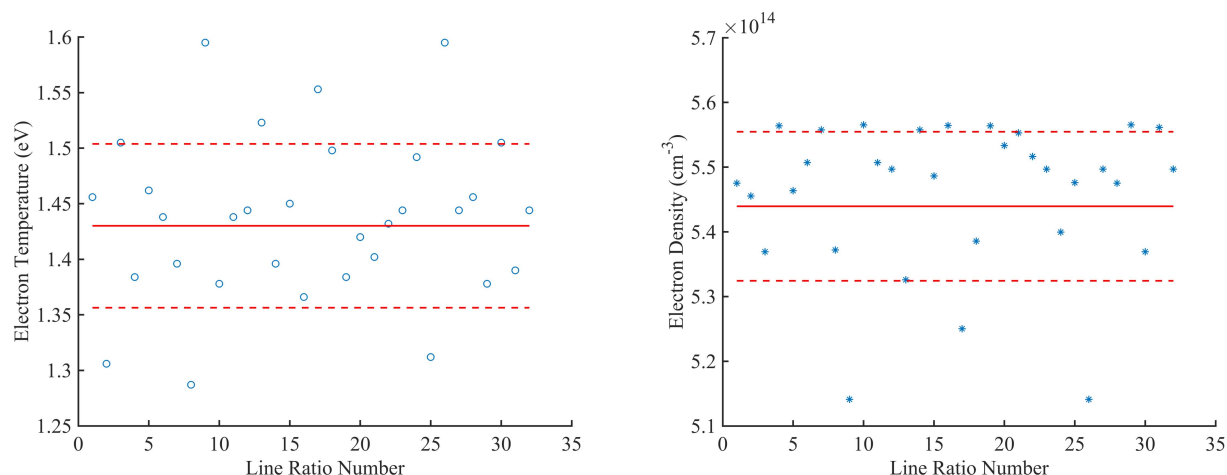


Fig. 21. Spread of T_e and n_e values from individual line ratios of a given emission spectrum (blue markers). T_e and n_e values and standard deviation from the averaged line ratio (solid and dotted red lines).

bound of 14% and 7% for electron temperature and density, respectively, it was justified to use T_e and n_e measurements from the averaged line ratio instead of individual line ratios for the time-resolved analysis.

The following additional uncertainties were estimated from literature: spectra distortion through the glass tube ($\sim 5\%$), wavelength and intensity calibration source and actual calibration ($\sim 3\%$), intensity calibration source and actual calibration from 300 to 750 nm ($\sim 5\%$), instrument broadening (1%), peak wavelength-matched intensities (5–10%), and PrismSPECT modeling (1–10%) [24], [26], [27], [38]. From all the uncertainties listed in this section, a maximum bound on the overall uncertainty for T_e and n_e , was, therefore estimated to be 27% and 23%, respectively.

V. CONCLUSION

This article explores the ability to use an ICCD-spectrometer assembly to obtain time-resolved spectroscopy data for nanosecond-pulsed plasmas. The emission data were analyzed with the line ratio method to determine the nanosecond time evolution of electron density and electron

temperature. The plasmas were generated using a wide range of operating conditions with varying discharge voltage, pulse frequency, and argon pressure. Results indicated that all generated plasmas had ionization and recombination times in the tens of nanoseconds, and trends about electron density and electron temperature were discovered.

While using OES with line ratio analysis to calculate plasma parameters is not new, using it to research plasmas on the nanosecond timescale is. The major contribution of this article was to measure and analyze the time evolution of plasma parameters through the lifetime of a pulsed, argon plasma discharge to increase understanding of nanosecond-pulsed plasma dynamics.

REFERENCES

- [1] S. Yang *et al.*, "Nanosecond pulsed plasma activated $C_2H_4/O_2/Ar$ mixtures in a flow reactor," *J. Propuls. Power*, vol. 32, pp. 1240–1252, Sep. 2016.
- [2] A. Roettgen, I. Shkurenkov, S. M. Simeni, I. V. Adamovich, and W. R. Lempert, "Time-resolved electron temperature and electron density measurements in a nanosecond pulse filament discharge in H_2 -He and O_2 -He mixtures," *Plasma Sources Sci. Technol.*, vol. 25, pp. 055008-1–055008-12, Aug. 2016.

- [3] X. Duten, D. Packan, L. Yu, C. O. Laux, and C. H. Kruger, "DC and pulsed glow discharges in atmospheric pressure air and nitrogen," *IEEE Trans. Plasma Sci.*, vol. 30, no. 1, pp. 178–179, Feb. 2002.
- [4] S. Hübner, J. M. Palomares, E. A. D. Carbone, and J. J. A. M. van der Mullen, "A power pulsed low-pressure argon microwave plasma investigated by Thomson scattering: Evidence for molecular assisted recombination," *J. Phys. D: Appl. Phys.*, vol. 45, no. 5, pp. 055203-1–055203-8, 2012.
- [5] X. Wen, Y. Xin, C. Feng, and H. Ding, "Simulations and measurement of electron energy and effective electron temperature of nanosecond pulsed argon plasma," *Plasma Sci. Technol.*, vol. 14, pp. 40–47, Jan. 2012.
- [6] G. A. Emmert and M. A. Henry, "Numerical simulation of plasma sheath expansion, with applications to plasma-source ion implantation," *J. Appl. Phys.*, vol. 71, no. 1, pp. 113–117, 1998.
- [7] A. Roettgen, I. Shkurenkov, S. M. Simeni, V. Petrishchev, I. V. Adamovich, and W. R. Lempert, "Time-resolved electron density and electron temperature measurements in nanosecond pulse discharges in helium," *Plasma Sources Sci. Technol.*, vol. 25, no. 5, pp. 055009-1–055009-14, 2016.
- [8] F. Chen, "Mini-course on plasma diagnostics," in *Proc. IEEE-ICOPS Meeting*, Jeju, Korea, Jun. 2003.
- [9] Y. Celik, M. Aramaki, D. Luggenhölscher, and U. Czarnetzki, "Determination of electron densities by diode-laser absorption spectroscopy in a pulsed ICP," *Plasma Sources Sci. Technol.*, vol. 20, pp. 015022-1–015022-13, Jan. 2011.
- [10] R. Manoharan, T. K. Boyson, and S. O'Byrne, "Time-resolved temperature and number density measurements in a repetitively pulsed nanosecond-duration discharge," *Phys. Plasmas*, vol. 23, no. 12, pp. 123527-1–123527-10, 2016.
- [11] B. T. Yee, B. R. Weatherford, E. V. Barnat, and J. E. Foster, "Dynamics of a helium repetitively pulsed nanosecond discharge," *J. Phys. D: Appl. Phys.*, vol. 46, no. 50, 2013, Art. no. 505204.
- [12] W. Zhou *et al.*, "Development of a nanosecond discharge-enhanced laser plasma spectroscopy," *Opt. Lett.*, vol. 36, no. 15, pp. 2961–2963, 2011.
- [13] *PI-MAX/PI-MAX2 System*, Princeton Instrum., Trenton, NJ, USA, Sep. 2011.
- [14] F. Schwirzke, M. P. Hallal, and X. K. Maruyama, "Explosive plasma formation on electrodes," in *Proc. 8th IEEE Int. Conf. Pulsed Power*, Jun. 1991, pp. 663–666.
- [15] C. Chan, "Experimental investigation of fast plasma production for the VAIPER antenna," M.S. thesis, Georgia Inst. Technol., Atlanta, GA, USA, 2017.
- [16] P. Singletary, "Optical characterization of a high speed plasma's electromagnetic properties," M.S. thesis, Georgia Inst. Technol., Atlanta, GA, USA, 2018.
- [17] *NSP-30/60/120-5/10/20/30-F/P/N-250/500 User's Manual*, Eagle Harbor Technol., Seattle, WA, USA, 2016.
- [18] I. Slobodov, "High voltage nanosecond pulse measurement techniques," Eagle Harbor Technol., Seattle, WA, USA, EHT Tech. Note #1, 2016.
- [19] H. R. Griem, *Principles of Plasma Spectroscopy*. Cambridge, U.K.: Cambridge Univ. Press, 2005.
- [20] J. Cooper, "Plasma spectroscopy," *Rep. Progr. Phys.*, vol. 29, no. 1, pp. 35–130, 1966.
- [21] M. Numano, "Criteria for local thermodynamic equilibrium distributions of populations of excited atoms in a plasma," *J. Quant. Spectrosc. Radiat. Transf.*, vol. 43, no. 4, pp. 311–317, 1990.
- [22] K. Kano, M. Suzuki, and H. Akatsuka, "Spectroscopic measurement of electron temperature and density in argon plasmas based on collisional-radiative model," *Plasma Sources Sci. Technol.*, vol. 9, no. 3, pp. 314–322, 2000.
- [23] B. Der Van Sijde, J. J. A. M. van der Mullen, and D. C. Schram, "Collisional Radiative Models in Plasmas," *Beiträge aus der Plasmaphysik*, vol. 24, no. 5, pp. 447–473, 1984.
- [24] S. Siepa, S. Danko, T. V. Tsankov, T. Mussenbrock, and U. Czarnetzki, "On the OES line-ratio technique in argon and argon-containing plasmas," *J. Phys. D: Appl. Phys.*, vol. 47, no. 44, pp. 445201-1–445201-17, 2014.
- [25] A. Bogaerts, R. Gijbels, and J. Vlcek, "Collisional-radiative model for an argon glow discharge," *J. Appl. Phys.*, vol. 84, no. 1, pp. 121–136, 1998.
- [26] X. M. Zhu, Y. K. Pu, N. Balcon, and R. Boswell, "Measurement of the electron density in atmospheric-pressure low-temperature argon discharges by line-ratio method of optical emission spectroscopy," *J. Phys. D: Appl. Phys.*, vol. 42, no. 14, Art. no. 142003, 2009.
- [27] X. M. Zhu, J. L. Walsh, W. C. Chen, and Y. K. Pu, "Measurement of the temporal evolution of electron density in a nanosecond pulsed argon microplasma: Using both Stark broadening and an OES line-ratio method," *J. Phys. D: Appl. Phys.*, vol. 45, no. 29, pp. 295201-1–295201-12, 2012.
- [28] R. W. P. McWhirter and A. G. Hearn, "A calculation of the instantaneous population densities of the excited levels of hydrogen-like ions in a plasma," *Proc. Phys. Soc.*, vol. 82, no. 5, pp. 641–654, 1963.
- [29] T. Fujimoto, "Kinetics of ionization-recombination of a plasma and population density of excited ions. II. Ionizing plasma," *J. Phys. Soc. Jpn.*, vol. 47, no. 1, pp. 265–281, 1979.
- [30] A. M. Gomes, "Criteria for partial LTE in an argon thermal discharge at atmospheric pressure; validity of the spectroscopically measured electronic temperature," *J. Phys. D: Appl. Phys.*, vol. 16, pp. 357–378, 1983.
- [31] H. R. Griem, *Spectral Line Broadening by Plasmas* (Pure and Applied Physics), vol. 39. New York, NY, USA: Academic, 1974.
- [32] S. Yugeswaran and V. Selvarajan, "Electron number density measurement on a DC argon plasma jet by stark broadening of Ar I spectral line," *Vacuum*, vol. 81, no. 3, pp. 347–352, 2006.
- [33] S. Djurović and N. Konjević, "On the use of non-hydrogenic spectral lines for low electron density and high pressure plasma diagnostics," *Plasma Sources Sci. Technol.*, vol. 18, no. 3, pp. 035011-1–035011-9, 2009.
- [34] G. V. Marr, *Plasma Spectroscopy*. Amsterdam, The Netherlands: Elsevier, 1968.
- [35] R. M. van der Horst, T. Verreycken, E. M. van Veldhuizen, and P. J. Bruggeman, "Time-resolved optical emission spectroscopy of nanosecond pulsed discharges in atmospheric-pressure N₂ and N₂/H₂O mixtures," *J. Phys. D: Appl. Phys.*, vol. 45, no. 34, pp. 345201-1–345201-12, 2012.
- [36] K. Honglertkongsakul, "Optical emission spectroscopy of argon plasma jet," *Adv. Mater. Res.* vol. 770, pp. 245–248, Sep. 2013.
- [37] C. A. Bye and A. Scheeline, "Saha–Boltzmann statistics for determination of electron temperature and density in spark discharges using an echelle/CCD system," *Appl. Spectrosc.*, vol. 47, no. 12, pp. 2022–2030, 1993.
- [38] *PrismSPECT User's Guide*, Prism Comput. Sci., Madison, WI, USA, 2018.
- [39] A. Kramida, Y. Ralchenko, and J. Reader. (2018) NIST Atomic Spectra Database (Ver. 5.5.6). NIST ASD Team, National Institute of Standards and Technology, Gaithersburg, MD, USA. Accessed: Aug. 7, 2018. [Online]. Available: <https://physics.nist.gov/asd>
- [40] R. Liu, Y. Liu, W. Jia, and Y. Zhou, "A comparative study on continuous and pulsed RF argon capacitive glow discharges at low pressure by fluid modeling," *Phys. Plasmas*, vol. 24, no. 1, 2017, Art. no. 013517.
- [41] J. B. Boffard, R. O. Jung, C. C. Lin, L. E. Aneskavich, and A. E. Wendt, "Argon 420.1–419.8 nm emission line ratio for measuring plasma effective electron temperatures," *J. Phys. D: Appl. Phys.*, vol. 45, no. 4, pp. 045201-1–045201-12, 2012.
- [42] J. R. Taylor, *An Introduction to Error Analysis: The Study of Uncertainties in Physical Measurements*, 2nd ed. Mill Valley, CA, USA: Univ. Science Books, 1982.



Connie Y. Liu received the B.S. degree in aerospace engineering from the Massachusetts Institute of Technology, Cambridge, MA, USA, in 2015, and the M.S. and Ph.D. degrees in aerospace engineering from the High-Power Electric Propulsion Laboratory, Georgia Institute of Technology, Atlanta, GA, USA, with a focus on electric propulsion and pulsed plasmas, in 2016 and 2019, respectively.

She is currently a Propulsion Development Engineer with Space Exploration Technologies, Hawthorne, CA, USA, where she is working on the Mars-bound Raptor engines. She specializes in the areas of electric propulsion, rocket combustion propulsion, and nanosecond pulsed plasmas.



Morris B. Cohen (Senior Member, IEEE) received the B.S. and Ph.D. degrees in electrical engineering from Stanford University, Stanford, CA, USA, in 2003 and 2010, respectively.

He served as a Research Associate with the Department of Electrical Engineering, Stanford University, until August 2013. From August 2012 to 2013, he was concurrently appointed as an AAAS Science and Technology Policy Fellow, serving at the National Science Foundation. In Fall 2013, he joined the School of Electrical Engineering,

Georgia Institute of Technology, Atlanta, GA, USA, as an Assistant Professor, where he has been an Associate Professor since August 2018. He has authored or coauthored 69 journal articles. His research focuses on low-frequency radio wave generation, propagation, detection, and data science, with applications to lightning physics, ionospheric remote sensing, space weather, and cybersecurity.

Dr. Cohen is currently the President-Elect of the Atmospheric and Space Electricity Section, American Geophysical Union. He is a 2014 Winner of the Santimay Basu Prize by the International Union of Radio Science, which is given once per three years to an under-35 scientist. He also won the 2015 Office of Naval Research (ONR) Young Investigator Winner, the 2017 NSF CAREER Award, and the Georgia Tech's Junior Faculty Teaching Excellence Award in 2018. He is an Associate Editor of Radio Science. He enjoys building wood-fired brick pizza ovens.



Mitchell L. R. Walker received the Ph.D. degree in aerospace engineering from the University of Michigan, Ann Arbor, MI, USA, where he specialized in experimental plasma physics and advanced space propulsion.

He is currently a Professor of aerospace engineering and an Associate Chair of graduate studies with the Georgia Institute of Technology, Atlanta, GA, USA, where he directs the High-Power Electric Propulsion Laboratory. His training includes rotations at Lockheed Martin and NASA Glenn Research

Center. In 2005, he founded the Electric Propulsion Program with the Georgia Institute of Technology. He has authored more than 120 journal articles and conference papers in electric propulsion and plasma physics. His research activities include Hall effect thrusters, gridded ion engines, magnetoplasmadynamic thrusters, diagnostics for plasma interrogation and thruster characterization, vacuum facility effects, helicon plasma sources, plasma-material interactions, and electron emission from carbon nanotubes. His primary research interests include both experimental and theoretical studies of advanced plasma propulsion concepts for spacecraft and fundamental plasma physics.

Dr. Walker is an Associate Fellow of AIAA. He has served as an Associate Editor for the American Institute of Aeronautics and Astronautics (AIAA) and on the Editorial Board of *Frontiers in Physics and Astronomy and Space Sciences—Plasma Physics* since 2015. He is the Chair of the AIAA Electric Propulsion Technical Committee. He delivered expert witness testimony *In-Space Propulsion: Strategic Choices and Options* to the Space Subcommittee Hearing—House of Representatives, Washington, DC, USA, in 2017, to help guide national investments in electric propulsion technology. He was a participant in the 2014 US National Academy of Engineering US *Frontiers of Engineering Symposium*. In 2015, he was the co-organizer for a focus session at the *Frontiers of Engineering Symposium*. He was a recipient of the Georgia Power Professor of Excellence Award, the AIAA Lawrence Sperry Award, the Air Force Office of Scientific Research Young Investigator Program Award, and the NASA Faculty Fellow Award.